EEET ECOLOGICAL ENGINEERING & ENVIRONMENTAL TECHNOLOGY

Ecological Engineering & Environmental Technology, 2025, 26(10), 218–230
https://doi.org/10.12912/27197050/211005
ISSN 2719–7050, License CC-BY 4.0

Received: 2025.08.22
Accepted: 2025.09.15
Published: 2025.10.01

Evaluation of thermal decomposition and ash transformation of water hyacinth pellets for sustainable bioenergy

Vo Cong Anh[1*], Pham Viet Hung[1], Do Thanh Tien[1], Tran Duc Hanh[1], Ve Quoc Linh[1], Khuong Anh Son[1], Trinh Ngoc Dat[2]

[1] Faculty of Engineering and Food Technology, University of Agriculture and Forestry, Hue University, Hue City, 530000, Vietnam
[2] Faculty of Physics, University of Science and Education, The University of Danang, Da Nang City, 550000, Vietnam
* Corresponding author's e-mail: voconganh@hueuni.edu.vn

ABSTRACT

Water hyacinth (*Eichhornia crassipes*), an invasive aquatic plant with exceptionally high yield, is increasingly considered a renewable energy feedstock. This study examines its thermal decomposition and ash evolution between 600 and 900 °C using thermogravimetric analysis (TG/DTG), scanning electron microscopy with energy-dispersive X-ray spectroscopy (SEM–EDX), and X-ray diffraction (XRD). TG/DTG identified three decomposition stages and a sticky-layer interval at 780–800 °C associated with alkali chloride melting. EDX results showed that K and Cl declined from 16.9 and 19.0 wt% at 600 °C to ≤ 2 wt% and ≤ 1.3 wt% at 900 °C, while Ca, Mg, and Fe increased. SEM analysis quantified a porosity maximum of 61.0% at 700 °C followed by a drop to 55.3% at 800 °C due to molten-phase infiltration. XRD revealed the progressive loss of sylvite and halite, the dominance of Fe_3O_4 at mid-range temperatures, and the emergence of $MgFe_2O_4$ spinel at 900 °C. The slagging index decreased steadily from 1.09 to 0.35 across the studied range. These results establish 780–800 °C as the sintering onset. For small-scale furnaces, maintaining bulk temperatures below 750 °C is recommended to minimize slagging and ensure stable operation.

Keywords: water hyacinth pellet, ash transformation, TGA, SEM-EDX, XRD.

INTRODUCTION

Water hyacinth (*Eichhornia crassipes*) is a rapidly proliferating aquatic plant recognized as one of the world's most invasive species. Its ability to double in biomass within as little as two weeks results in exceptionally high yields. Although often treated as an unwanted weed, this biomass can serve as a valuable renewable energy resource. Its use not only helps to control uncontrolled spread but also contributes to sustainable energy production (Gaurav et al., 2020; Li et al., 2021). Converting the harvested material into pellets enhances fuel quality by lowering moisture content and raising bulk density (Sukarta et al., 2023). In practice, this makes transport and storage more economical than handling the raw, bulky form (He et al., 2024; Marczak, 2020). For biomass with high moisture content, pelletization has been shown to cut transport and storage costs from roughly 40–60% down to 15–30% of the total supply chain. This cost reduction enables more efficient use in small-scale combustion devices, including household pellet stoves and farm-scale boilers (Onyari et al., 2024; Yue et al., 2025).

Small-scale furnaces and boilers that rely on biomass pellets usually operate at combustion chamber temperatures of 600–900 °C, which are lower than those in large industrial boilers (Mack et al., 2024; Rabaçal et al., 2013; Stanisławski et al., 2022). Water hyacinth pellets can supply useful heat under such conditions. However, their combustion behavior differs strongly from that

of wood pellets and other low-ash biomasses because of their inherently high ash fraction. On a dry-weight basis, water hyacinth typically contains 12–27 wt% ash, in sharp contrast to the < 5 wt% commonly reported for woody biomass. This ash is rich in potassium (K), chlorine (Cl), calcium (Ca), silicon (Si), and phosphorus (P) derived from the plant's growth environment (Lara-Serrano et al., 2016). During combustion, such composition predisposes the ash to slagging and fouling. Potassium and chlorine readily form low-melting compounds such as potassium chloride (KCl) and potassium carbonate (K_2CO_3) that can deposit on heat-transfer surfaces, forming sticky layers. High Cl and K contents are strongly correlated with ash deposition (Johansen et al., 2011; Kuswa et al., 2024). Additionally, volatilized chlorine from KCl or hydrochloric acid (HCl) in the flue gas can accelerate corrosion of downstream metallic components (Hu et al., 2023; Luan et al., 2025), increasing maintenance costs and causing unscheduled shutdowns (Chen et al., 2021; Król et al., 2022).

However, despite these studies, critical knowledge gaps remain. Prior work seldom quantifies surface porosity and particle necking from SEM or the amorphous fraction from XRD, nor integrates these morphological indicators with alkali ratios to pinpoint the onset of sticky layer formation during ash sintering. Furthermore, few studies couple elemental retention/volatilization fractions (e.g., K, Cl) with mineralogical phase evolution to define a critical sintering window for alkali-rich aquatic biomass. This lack of integrated, temperature-resolved analysis constrains the ability to establish reliable slagging thresholds and to optimize furnace operation.

Therefore, this study aims to: (i) quantify surface porosity and particle necking from SEM images at different combustion temperatures; (ii) estimate amorphous fraction and perform Rietveld phase quantification from XRD patterns; (iii) indicate ash melting problems; and (iv) correlate these metrics to identify the critical sintering window for water hyacinth pellet ash. The outcomes will provide a robust scientific basis for designing suitable combustion systems, optimizing operational temperatures in sustainable applications of water hyacinth.

MATERIALS AND METHODS

Materials

Water hyacinth (*Eichhornia crassipes*), including roots, stems, and leaves, was harvested from the Ngu Ha River, Hue City, Vietnam. The fresh biomass was washed to remove debris, chopped into 3–5 cm pieces, sun-dried for 2–3

Figure 1. Main steps in the pelletization process

days to reduce moisture from 90 % to 30 %, then oven-dried at 80 °C to a moisture content of 12 ± 2%. The dried biomass was milled to a particle size ≤ 2 mm, as this particle size yielded optimal pellet quality in preliminary trials. Pelletization was carried out on a hydraulic press with a die diameter of 10 mm at 150 MPa, without any external binders; heat and pressure during compaction mobilized lignin to act as a natural binder. The resulting pellets had a bulk density of 1186 ± 10 kg m^{-3} and mechanical durability > 95 %, meeting ISO 17831-1:2015 standards. Pellets were sealed in airtight polyethylene bags before analysis. Figure 1 presents the main steps for processing the water hyacinth pellets in this study.

The fundamental properties of the water hyacinth pellets are given in Table 1. Proximate analysis showed: moisture 13.3%, ash 14.0%, volatile matter 59.0%, fixed carbon 13.7% (all wt%, db). Ultimate analysis (wt%, db) gave: C 33.50%, H 4.64 %, N 1.04%, O by difference. The higher heating value (HHV) was 13.9 MJ kg^{-1} (PARR 6400). The relatively high ash content (14 wt%).

For ash preparation, 5.0 g of pellets were placed in porcelain crucibles and ashed in a muffle furnace (Nabertherm LT5/13/C450). The temperature was increased to 250 ± 5 °C at 10°C min^{-1} and held for 1 h to remove volatiles. The temperature was then ramped to 600, 700, 800, and 900°C at the same rate, with a residence time of 6 h at each temperature to ensure complete combustion and a stable ash residue (Racero-Galaraga et al., 2024). The ash yield at each temperature was determined gravimetrically. This baseline yield was used for calculating retention and volatilization fractions of K and Cl in subsequent analyses. After holding, the furnace was switched off and cooled naturally to room temperature before sample collection.

Analysis methods

TGA analysis

Thermogravimetric analysis (TGA) was performed to characterize the thermal decomposition behavior of water hyacinth pellets. Measurements were conducted on a Linseis TGA PT1600 (Linseis, Germany). Approximately 25 mg of milled pellet (≤1 mm) was loaded into an open, clean crucible and equilibrated at ambient temperature. The furnace was continuously purged with high-purity nitrogen to ensure an inert atmosphere. Samples were heated from room temperature to 1000 °C at a constant heating rate of 20 °C min^{-1}.

SEM–EDX analysis

The morphology and elemental composition of water hyacinth ash at 600, 700, 800, and 900 °C were examined using a scanning electron microscope (SEM, JSM-IT200, JEOL Ltd., Japan) operated at 15 kV accelerating voltage. Before imaging, samples were oven-dried at 80 °C

Table 1. Fundamental properties of water hyacinth pellets used in this study

Parameter	Unit	Value (mean ± SD)	Method
Proximate analysis:			
– Moisture (M)	wt% (db)	13.3 ± 0.2	ISO 18134-1:2015
– Ash (A)	wt% (db)	14.0 ± 0.3	BS EN ISO 18122:2015
– Volatile matter (VM)	wt% (db)	59.0 ± 0.5	ISO 17225-1:2021
– Fixed carbon (FC)	wt% (db)	13.7 ± 0.4	ISO 17225-1:2021
Ultimate analysis:			
– Carbon (C)	wt% (db)	33.50 ± 0.15	BS EN ISO 16948:2015
– Hydrogen (H)	wt% (db)	4.64 ± 0.05	BS EN ISO 16948:2015
– Nitrogen (N)	wt% (db)	1.04 ± 0.02	BS EN ISO 16948:2015
– Oxygen (O)	wt% (db)	60.82	By difference
Energy property			
– HHV	MJ kg^{-1}	13.9 ± 0.1	PARR 6400
Physical properties:			
– Particle size	mm	≤ 2	Sieve analysis
– Bulk density	kg m^{-3}	1186 ± 10	ISO 17828:2015
– Mechanical durability	%	> 95	ISO 17831-1:2015

Note: The results are the average values of three measured samples.

to remove residual moisture, mounted on aluminum stubs with carbon adhesive tabs, and sputter-coated with a 10 nm gold layer to minimize charging. Elemental composition was determined with the energy-dispersive X-ray spectroscopy (EDX) system integrated into the SEM, which provided both qualitative and semi-quantitative data on the main inorganic constituents. For each condition, at least three representative regions were analyzed, and the values were averaged to yield one dataset. Surface porosity was subsequently quantified from high-magnification SEM images (≥ ×1000) using binary thresholding in ImageJ (NIH, USA), with porosity (%) calculated as the pore area relative to the total analyzed area.

XRD analysis

The crystalline phases of water hyacinth ash and their transformations with temperature were characterized using an X-ray diffractometer (D8 Advance, Bruker, Germany) operated at 40 kV and 40 mA with Cu-Kα radiation (λ = 1.5406 Å). Samples were gently ground to pass a 63 μm sieve before measurement. Data were collected over a 2θ range of 10–80° at a scan rate of 10° min^{-1}. Phase identification was performed using the ICDD PDF-4+ database in MDI Jade 6.5 software. In addition to qualitative identification, relative changes in the amorphous phase content with temperature were estimated from the background hump area (20–35° 2θ) using the integrated peak method.

Porosity quantification from SEM images

Surface porosity in water hyacinth ash was measured from high-magnification SEM micrographs using a binary image segmentation method. The grayscale SEM images were converted into binary masks through adaptive thresholding, where pore regions appeared as white pixels and the solid matrix as black. Segmentation settings were carefully adjusted so that particle edges and fine pore structures could be distinguished with fidelity. Porosity was then determined from the ratio of pore pixels to the total number of pixels in the image, expressed as:

$$Porosity\ (\%) = \\ = \frac{N_{white\ pixels}}{N_{total\ pixels}} \times 100 \quad (1)$$

where: $N_{white\ pixels}$ is the number of pixels classified as pores and $N_{total\ pixels}$ is the total pixel count. Several fields of view were evaluated at each combustion temperature to minimize local bias, and an average porosity value was reported. This metric accounts for both inter-particle voids and intra-particle cavities at the chosen magnification, thus providing a quantitative descriptor of surface openness. When these porosity data are interpreted alongside SEM morphology, XRD phase composition, and alkali content obtained from EDX, they yield a more reliable indicator of sintering onset and slagging tendency in biomass ash.

RESULTS AND DISCUSSION

Thermal decomposition (TG/DTG)

The TG/DTG curve of water hyacinth pellets is shown in Figure 2. Three distinct stages of thermal decomposition are identified. Below 200 °C, a small mass loss of 5–7% with a DTG shoulder corresponds to the evaporation of physically bound moisture. Between 200 and 350 °C, the sharp DTG peak (Tp) and 50% weight loss reflect the rapid volatilization of hemicellulose, cellulose, and part of lignin. This is the primary devolatilization stage, generating the largest flux of combustible gases. Similar behavior has been reported for rice husk, wheat straw, sorghum straw, and corn stover (Czekała et al., 2025; Ríos-Badrán et al., 2020).

Between 350 and 600 °C, the TG curve declines slowly, and the DTG response shows only small amplitudes. This behavior reflects the gradual decomposition of refractory lignin together with the onset of partial mineral changes. Once the temperature rises above 700 °C, the TG trace levels off, with less than 3 % additional mass loss recorded up to 900 °C. The flat segment indicates that nearly all organic matter has already been consumed, leaving mineral ash as the primary residue. At the same time, the DTG baseline remains close to zero, confirming that further devolatilization is negligible.

Within this plateau region, a narrow sticky-layer window emerges between 780 and 800 °C. In this range, the TG curve remains flat, showing no further release of volatiles. However, SEM observations (discussed in detail later, Figure 5, Table 2) reveal active morphological

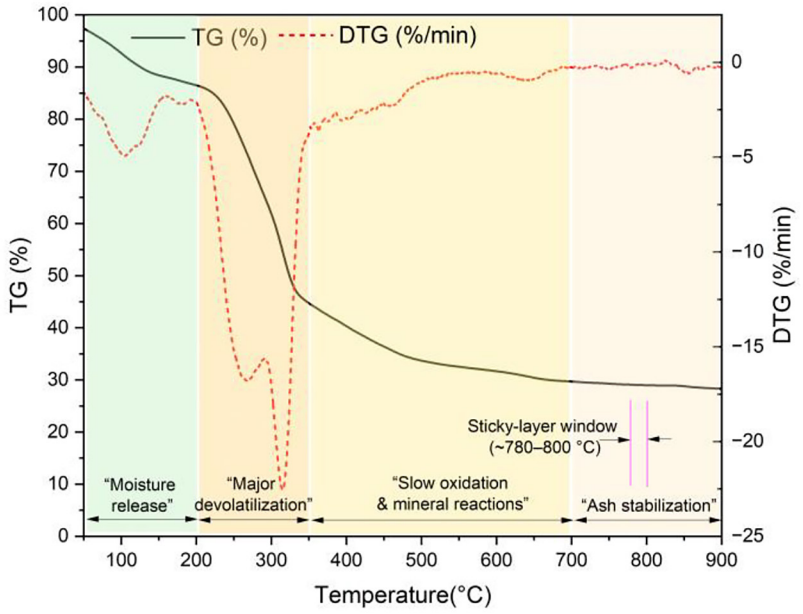

Figure 2. TG/DTG profiles of water hyacinth pellets showing thermal decomposition stages, high-temperature plateau (> 700 °C), and sticky-layer window (780–800 °C)

transformations in the ash, including particle necking and the formation of molten salt bridges. These features are consistent with the melting of low-temperature eutectics such as KCl (melting point ~776 °C) and mixed alkali silicates, which induce sintering without measurable mass loss. From a practical standpoint, this temperature range represents the most critical stage for slag formation. Within it, low-viscosity molten layers can quickly cause ash particles to coalesce into stable deposits. Recognizing this window is therefore essential for small-scale combustion control: furnace operation should remain below 750 °C to avoid the sticky zone, whereas sustained exposure above 800 °C promotes irreversible sintering and markedly elevates the risk of slagging.

Ash chemistry and slagging indicators

The elemental composition of water hyacinth ash at different combustion temperatures is presented in Figure 3. Volatile elements (K, Cl, Na, P) are shown in Figure 3a, while refractory elements (Ca, Fe, Mg, Si) are plotted in Figure 3b. These two groups exhibit opposite trends between 600 and 900 °C. In the volatile group, K and Cl are initially high (16.9 and 19.0 wt% at 600 °C) but decline sharply to 2.0 and 1.3 wt% at 900 °C, corresponding to reductions of 88% and 93%. This decline reflects the evaporation of KCl and NaCl salts at medium–high temperatures, the main source of low-melting liquid phases in biomass ash (Chen et al., 2016; Hedayati et al., 2022). Na remains consistently low (1.3–2.5 wt%), while P decreases from 5.0 wt% to 3.4 wt% at 700 °C, then rises to 6.1 wt% at 900 °C due to relative concentration effects after volatilization (Wu et al., 2011).

In contrast, refractory elements enrich with temperature. Calcium increases consistently from 13.3 wt% at 600 °C to 22.0 wt% at 900 °C, reflecting the thermal stability of CaO and Ca–silicate phases. Magnesium remains between 6.2 and 7.4 wt% below 700 °C, decreases slightly to 5.8 wt% at 800 °C, and then rises again to 9.3 wt% at 900 °C. Silicon content is low (1.6–2.5 wt%) across the range, though a minor enrichment is observed at higher temperatures. Iron shows the largest variation: it rises from 4.1 wt% at 600 °C to 17.4 wt% at 800 °C before falling to 6.7 wt% at 900 °C, a trend that points to redistribution into refractory phases or agglomeration of particles (Li et al., 2022; Yilmaz et al., 2021).

These results indicate that for small-scale furnaces, maintaining operation within 700–800°C is a favorable range. In this interval, K and Cl levels fall by more than 50%, reducing the formation of alkali–halogen melts, while Ca, Mg, and Fe remain sufficiently abundant to stabilize the ash matrix. Strict temperature uniformity must be maintained because localized overheating facilitates the reappearance of alkali-rich liquid

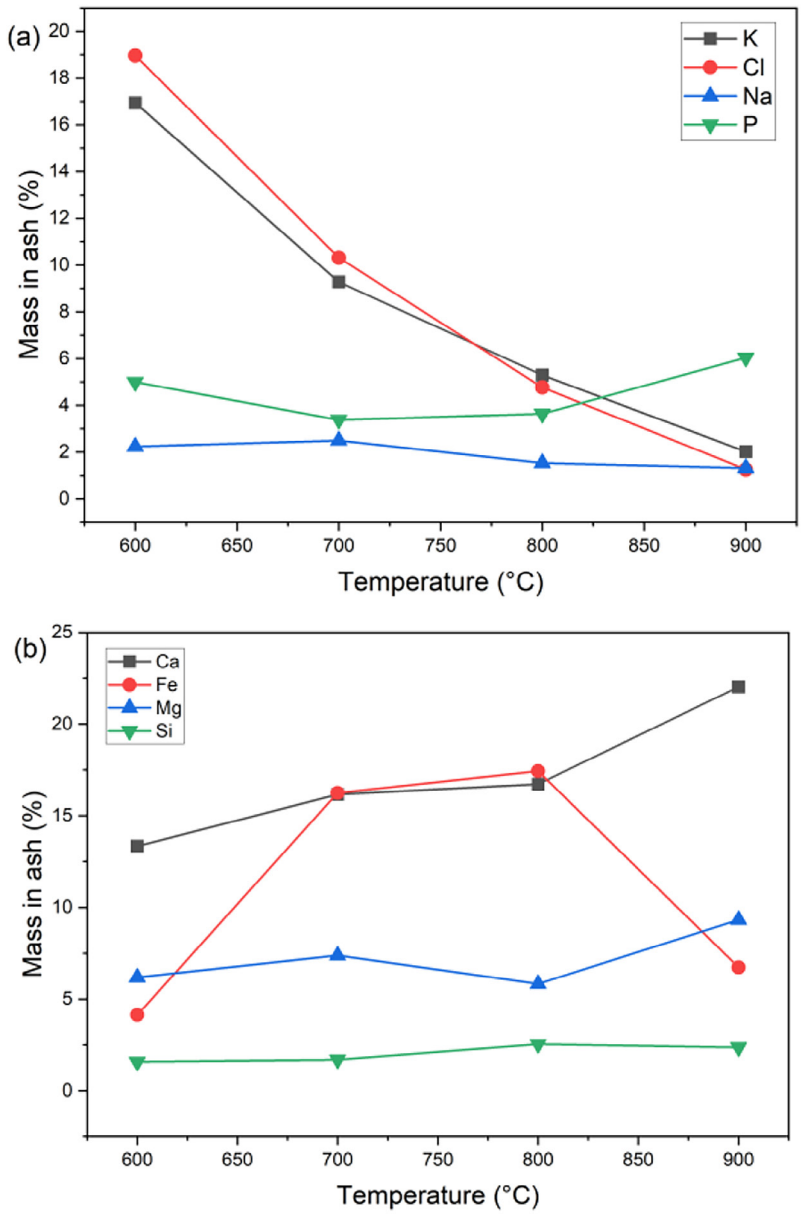

Figure 3. Elemental composition of water hyacinth ash at 600–900°C, from EDX analysis (a) volatile elements K, Cl, Na, and P; (b) refractory elements Ca, Fe, Mg, and Si

phases, thereby intensifying slagging and corrosion (He et al., 2022; Smołka-Danielowska and Jabłońska, 2022).

The impact of these compositional shifts on slagging propensity was further assessed using the slagging index (SI). Ca and Mg typically increase ash-melting temperature, whereas Si with K reduces it (Hrbek et al., 2021; Sommersacher et al., 2012). To quantify this effect, SI was calculated using Equation 2, as proposed by Sommersacherr et al. (2012):

$$SI = \frac{Si+P+K}{Ca+Mg} \text{ [mol/mol]} \quad (2)$$

As shown in Figure 4, SI decreased from 1.09 at 600 °C to 0.35 at 900 °C. A high SI reflects greater risk of phosphate, silicate, and alkali-salt deposition, since K, Na, and P readily form low-melting eutectics. The observed decline is consistent with K and Cl volatilization and the relative enrichment of Ca and Mg, which neutralize acidic components. Recent studies confirm that SI < 2 represents a reliable safety threshold for K-rich biomass (Lachman et al., 2021; Sommersacher et al., 2012). Accordingly, the intermediate SI values at 700–800 °C, together with the > 50% reduction of K and Cl (Figure 3a), identify

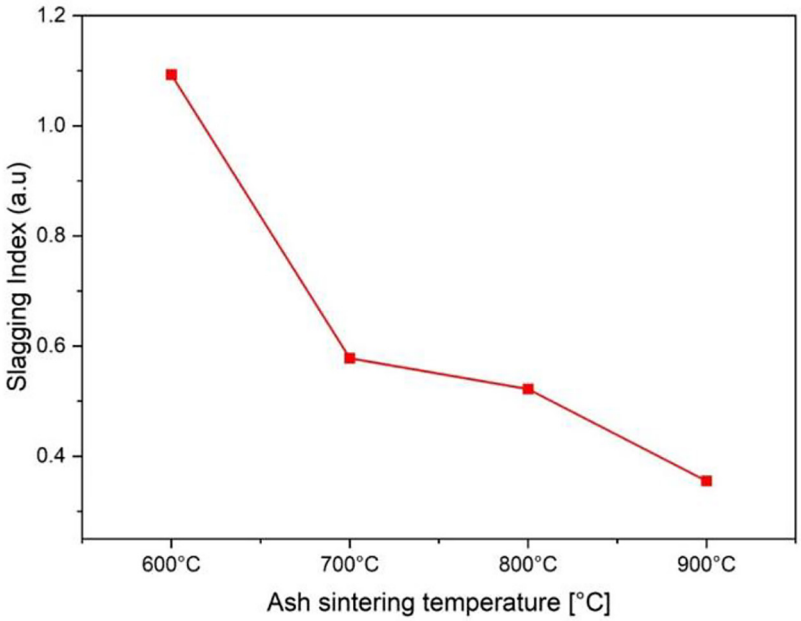

Figure 4. Slagging index versus ash sintering temperature

this window as the most favorable range for minimizing slagging and ensuring stable operation in small-scale combustion systems.

Morphology and microstructure observed by SEM

The SEM sequence (Figure 5) and porosity analysis (Figure 6, Table 2) reveal a clear temperature-driven transformation of water hyacinth ash between 600 and 900 °C. At 600 °C (Figure 5a), the ash is composed of fine, irregular fragments with skeletal, plant-derived textures and rough surfaces. Molten-phase bonding is negligible, and porosity remains relatively high (42.8%, Table 2). This friable morphology reflects a state where organics have been largely devolatilized but alkali salts remain solid, consistent with TG/DTG data showing that mass loss plateaus only at higher temperatures (Beidaghy Dizaji et al., 2022). By 700 °C (Figure 5b), porosity increases to a peak of 61.0% (Figure 6, Table 2), and SEM images show a more open, loosely connected structure with initial neck formation between particles. Despite the higher porosity, the onset of necking indicates the transition to a "pre-sticky" regime in which partial melting promotes early-stage consolidation of the ash framework.

A distinct change occurs between 780 and 800 °C, matching the sticky-layer range from TG/DTG analysis (Section 3.1). At this point, porosity falls to 55.3% (Figure 6, Table 2). SEM images (Figure 5c) show smooth, glass-like bridges that link nearby grains. The appearance signals continuous molten films with low viscosity. These films are dominated by KCl, NaCl, and mixed alkali silicates (Abioye et al., 2024). Other SEM views reveal droplets and voids left by trapped gases. Such features are typical of alkali melts moving into the ash structure (Luan et al., 2025; Wang et al., 2024). The liquid phases pass through pore channels, connect particles, and improve adhesion. Importantly, this takes place without obvious bulk mass loss. EDX data confirm the same trend. Volatile K and Cl decrease from 16.9 wt% and 19.0 wt% at 600 °C to ≤ 2 wt% and ≤ 1.3 wt% at 900 °C (Figure 3a). In contrast, refractory elements such as Ca, Mg, and Fe remain and enrich the residual matrix (Figure 3b). This balance explains why the system gains stability at higher temperature.

At 900 °C (Figure 5d), the ash consolidates into dense, slag-like agglomerates. The surface becomes smoother, while porosity levels off at about 58.8% (Figure 6, Table 2). Traces of the original plant microstructure are no longer visible. Instead, the solid phase develops into a continuous glassy framework. EDX measurements reveal an accumulation of Ca, Mg, and Fe. This composition points to the growth of refractory spinel phases such as $MgFe_2O_4$ and Ca–Fe oxides. These phases are recognized for producing deposits that are both highly adhesive and

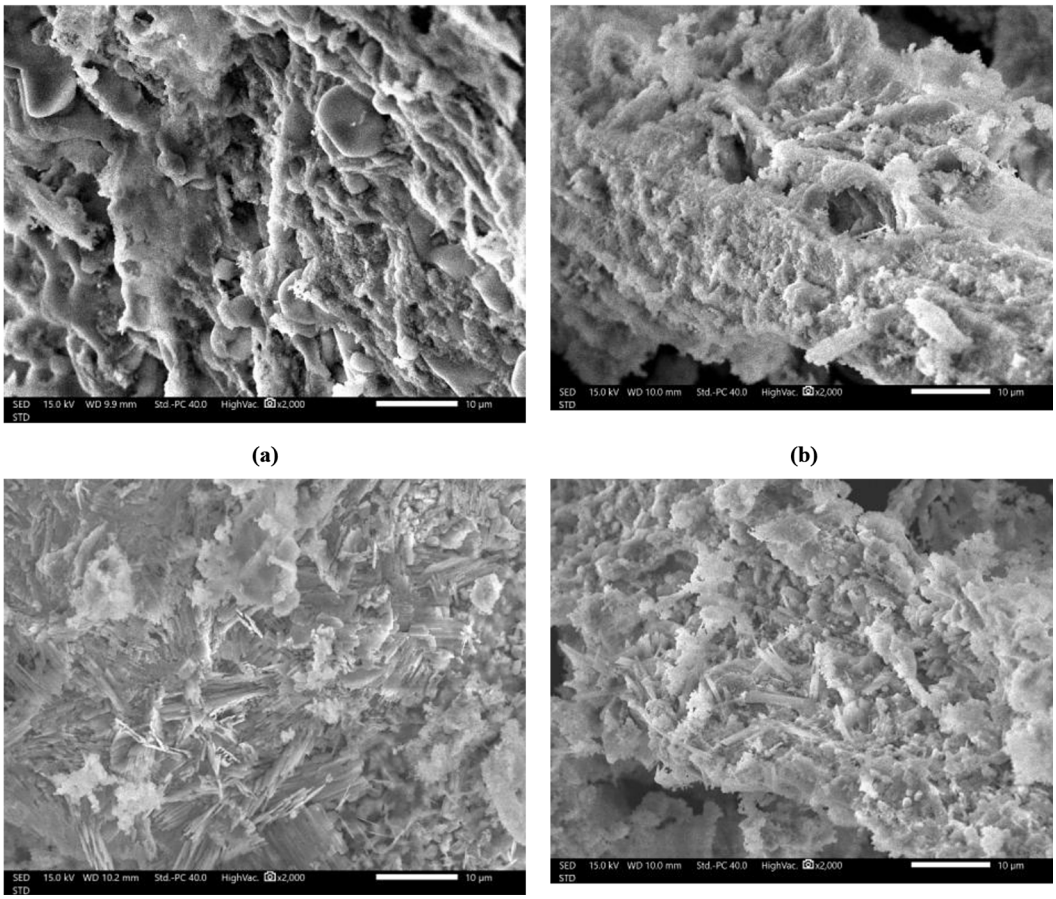

Figure 5. SEM images of a water hyacinth ash at different combustion temperatures:(a) 600 °C, (b) 700 °C, (c) 800 °C, and (d) 900 °C

mechanically strong, making them resistant to removal (Vassilev et al., 2017).

Below 750 °C, the ash retains a porous and friable structure, which corresponds to a low risk of slagging under steady furnace operation. Once the temperature passes 780 °C, the material enters the sticky range, where molten salts penetrate the matrix and cause rapid adhesion. When heating continues beyond 800 °C, the process leads to irreversible sintering and the build-up of slag-like masses. From a practical standpoint, SEM observations offer a useful warning. Small furnaces should be run below 750 °C and, more importantly, avoid hot spots that push the local temperature higher. Such control reduces the chance of slagging, lengthens the time between maintenance stops, and supports reliable system performance (Chen et al., 2016; Yilmaz et al., 2021).

Phase evolution from XRD

The XRD patterns of water hyacinth ash at 600–900 °C (Figure 7) demonstrate a systematic phase transformation, shifting from alkali salt–dominated assemblages toward refractory oxides and spinels as thermal severity increased.

At 600 °C, sharp peaks of KCl (sylvite) and NaCl (halite) were dominant, consistent with the high K and Cl contents measured by EDX (Figure 3a) and in line with earlier reports on aquatic biomass ashes (Du et al., 2014; Vassilev et al., 2017). These salts, with melting points near 770–800 °C, are highly problematic because they volatilize or melt within the "sticky-layer" window, forming low-viscosity films that promote adhesion to heat exchange surfaces. This explains why the slagging index (SI, Section 3.2) was highest at this stage (SI ≈ 1.09), indicating severe deposition risk when the ash mineralogy is dominated by alkali halides.

Between 700 and 800 °C, the diffraction peaks of KCl and NaCl drop sharply, confirming volatilization of the alkali salts. At the same time, the peaks of Fe_3O_4 (magnetite) increase in intensity, consistent with the relative enrichment of Fe-rich phases as salts are depleted. Quartz

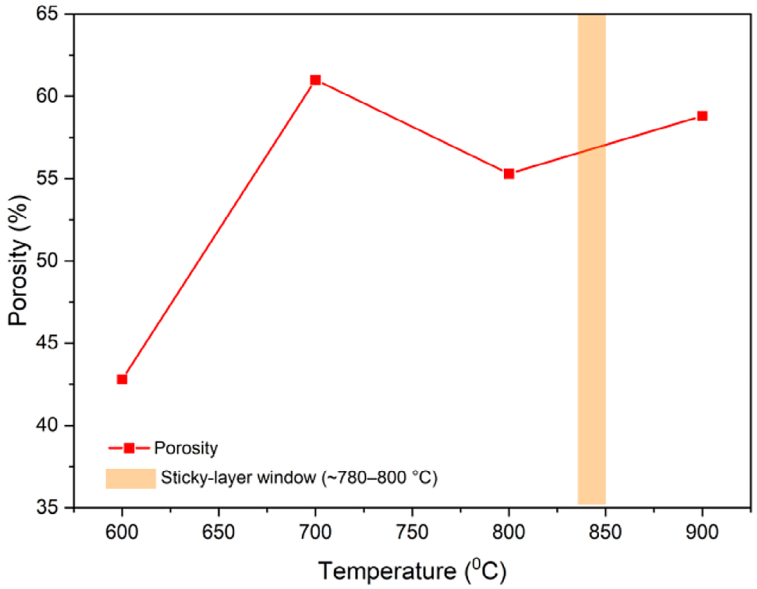

Figure 6. Surface porosity vs. temperature from SEM image analysis

Table 2. SEM-based morphology metrics and implications

T (°C)	Qualitative morphology (SEM)	Porosity (%)	Necking freq.	Agglomerate D50 (μm)	Operational implication
600	Loose, porous, skeletal	42.8	Rare	Low	Low slag risk; easy removal
700	Discrete grains + first necks	61.0	Moderate	Low	Entry to sticky regime
800	Partially fused, glassy bridges	55.3	High	↑	Peak stickiness (KCl/NaCl molten)
900	Dense, slag-like masses	58.8	Very high	Large	Severe sintering; hard deposits

(SiO_2) is still observed at all temperatures, which shows that the siliceous fraction reacts only weakly within this window. The parallel loss of alkali salts and the marked increase in porosity (from 43% to > 60%, Table 2) imply that volatile release and breakdown of unstable minerals leave behind a loose, open framework. Such a framework is less prone to slagging. At 800 °C, SI decreased to 0.52, confirming a substantially lower slagging potential. Importantly, although the sticky-layer window (780–800 °C) was reached, the ash remained friable, and molten films were transient rather than fully consolidated.

At 900 °C, alkali salts had nearly disappeared from the diffraction patterns, while $MgFe_2O_4$ (magnesioferrite) emerged for the first time. This phase forms via solid-state reaction between Fe_3O_4 and MgO derived from Mg-bearing minerals. The substitution of Fe^{2+} by Mg^{2+} at octahedral sites stabilizes the spinel lattice (Kaknics et al., 2016). With its very high melting point (> 1800°C) and chemical inertness, $MgFe_2O_4$ represents a refractory sink for Fe and Mg, reducing the availability of fluxing agents and thereby lowering slagging risk. The SI reached its lowest value at this stage (0.35), reflecting a mineralogy dominated by stable oxides and spinels.

The XRD findings align well with SEM–EDX and SI observations. Together, they highlight 780–800 °C as the sticky-layer interval, where molten alkali phases reach their maximum and slagging risk is greatest. At 900 °C, the ash turns refractory and shows reduced slagging tendency. However, furnace operation above 800 °C is not advisable. Energy demand rises, and the shift from a porous to a sintered structure creates deposits that are dense, strong, and resistant to removal. For this reason, keeping bulk combustion temperatures below 750 °C offers the best balance. It promotes alkali loss without excessive sintering, lowers slagging potential, and supports stable long-term operation.

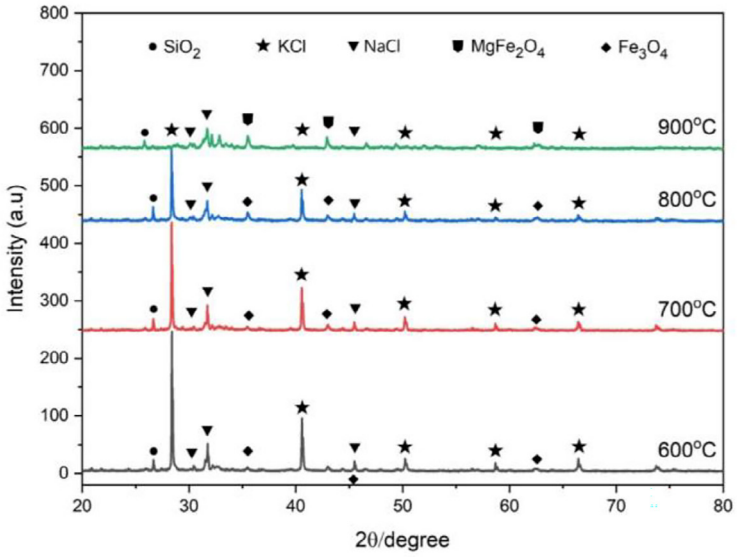

Figure 7. XRD patterns of water hyacinth ash at 600 °C, 700 °C, 800 °C, and 900 °C

Practical implications for small-scale combustion

Integration of TG/DTG, EDX, XRD, porosity, and slagging index data at 600–900 °C allows the design implications for small-scale (fixed-bed/pellet) incinerators to be structured into five decision groups:

a) Combustion chamber temperature and residence time

Between 700 and 800 °C, K and Cl are expelled from the ash primarily as volatilized KCl/NaCl, with release rates accelerating in the 700–900 °C interval. This corresponds to the sharp decline of K, Cl in EDX (Figure 3a) and weakening of halide peaks in XRD (Figure 7). Operating the bed at 780–820 °C maximizes halide removal while avoiding excessive retention of ash in the sticky-layer window (780–800 °C). Similar temperature–time dependencies of K release have been reported for herbaceous biomass (Pio et al., 2020; Zhang et al., 2023).

b) Heat-exchange surface temperature control

Deposition proceeds through sequential condensation, adhesion, and growth, with gaseous KCl forming the initial sticky layer. Field data show severe condensation on cold metal surfaces (~100 °C). To mitigate this, a refractory throat/riser section should be inserted before heat recovery units, allowing KCl vapors to bypass the cold surface zone. Smooth hot surfaces or a pre-cyclone can further reduce particle impaction (Weber et al., 2021; Zhang et al., 2020).

c) Ash layer management on grate

Although the slagging index decreases with temperature (SI: 1.09 → 0.35), SEM (Figure 5) shows partial sintering and necking near 780–800 °C, where KCl remains active. Grate design should therefore: (i) maintain grate surface < sticky-layer temperatures via air cooling, (ii) incorporate moving or vibrating grates to disrupt ash bridges, and (iii) ensure even primary and secondary air distribution to prevent localized overheating. These measures align with observed KCl-mediated sintering physics (Zhang et al., 2020).

d) Use of low-cost additives ("de-sticking")

Aluminosilicates (kaolin, bentonite, halloysite) capture alkalis and form high-melting aluminosilicates, reducing Cl in the ash and raising softening temperature. Laboratory and pilot-scale trials confirm significant mitigation of KCl slagging. For water hyacinth, 1–3 wt% kaolin addition (or a thin bed coating) is recommended (Mörtenkötter et al., 2024).

e) Heat-exchange material selection by ash mineralogy

At 800–900 °C, XRD shows formation of Fe–Mg spinels ($MgFe_2O_4$) and magnetite—refractory phases with low stickiness compared to alkali halides. Similar spinel stabilization has been reported in Mg–Fe-rich wastes (Mörtenkötter et al., 2024). This supports a staged layout: complete

ash transformation in a hot refractory chamber, followed by gas transfer through a cyclone/deflector before contact with metal heat exchangers.

f) System design synthesis

An optimized kiln for water hyacinth pellets should comprise: (i) refractory-lined primary chamber with bed temperature controlled at 780–820 °C under uniform air supply; (ii) a short secondary oxidation zone above the bed to complete gas combustion without prolonged ash residence; (iii) a refractory throat to suppress KCl condensation, leading into a small cyclone; (iv) downstream heat exchangers positioned in the salt-depleted gas stream; (v) automatic ash vibration or drainage to disrupt early sintering. This configuration is consistent with the ash transformation pathways identified here and with recent deposition models for alkali-rich biomass (Abioye et al., 2024; Trinh et al., 2024).

CONCLUSIONS

This work examined the thermal decomposition, ash behavior, and phase evolution of water hyacinth pellets between 600 and 900 °C using TG/DTG, SEM–EDX, and XRD. A narrow sticky-layer interval was identified at 780–800 °C. Within this window, molten alkali chlorides and silicates initiated rapid sintering, though bulk mass remained unchanged. EDX measurements confirmed an 88–93% depletion of K and Cl, clear evidence for volatilization of low-melting salts.

SEM results show that porosity reached its highest level near 700 °C. At 800 °C, this trend reversed: pores became partly filled and smooth glassy necks developed, marking the shift toward molten-phase consolidation. The XRD patterns support this sequence. Peaks assigned to KCl and NaCl weakened progressively, Fe_3O_4 signals became stronger, and by 900 °C the emergence of $MgFe_2O_4$ spinel was clearly detected. Across this range, the slagging index fell from 1.09 to 0.35, pointing to a shift from salt-rich, adhesive assemblages to more refractory oxide–spinel phases.

Taken together, the results show that 780–800 °C is the most critical zone where slagging is most likely. For small-scale systems, keeping bulk temperatures below 750 °C is the most effective way to limit sticky-layer growth. Operation beyond 820 °C encourages refractory spinel development but, if ash residence is prolonged, also risks irreversible sintering. In practice, these insights offer a quantitative basis for adjusting combustion strategies when using K–Cl-rich aquatic biomass fuels.

Acknowledgement

We gratefully acknowledge all participants for their valuable contributions to this study. We also extend our sincere thanks to Hue University for providing financial support for this research (Grant No. DHH2023-02-170).

REFERENCES

1. Abioye, K. J., Harun, N. Y., Sufian, S., Yusuf, M., Jagaba, A. H., Ekeoma, B. C., Kamyab, H., Sikiru, S., Waqas, S., Ibrahim, H. (2024). A review of biomass ash related problems: Mechanism, solution, and outlook. *Journal of the Energy Institute*, *112*, 101490. https://doi.org/https://doi.org/10.1016/j.joei.2023.101490
2. Beidaghy Dizaji, H., Zeng, T., Hölzig, H., Bauer, J., Klöß, G., Enke, D. (2022). Ash transformation mechanism during combustion of rice husk and rice straw. *Fuel*, *307*, 121768. https://doi.org/https://doi.org/10.1016/j.fuel.2021.121768
3. Chen, C., Bi, Y., Huang, Y., & Huang, H. (2021). Review on slagging evaluation methods of biomass fuel combustion. *Journal of Analytical and Applied Pyrolysis*, *155*, 105082. https://doi.org/https://doi.org/10.1016/j.jaap.2021.105082
4. Chen, C., Yu, C., Zhang, H., Zhai, X., Luo, Z. (2016). Investigation on K and Cl release and migration in micro-spatial distribution during rice straw pyrolysis. *Fuel*, *167*, 180-187. https://doi.org/https://doi.org/10.1016/j.fuel.2015.11.030
5. Czekała, W., Frankowski, J., Sieracka, D., Pochwatka, P., Kowalczyk-Juśko, A., Witaszek, K., Dudnyk, A., Zielińska, A., Wisła-Świder, A., Dach, J. (2025). The energy efficiency analysis of sorghum waste biomass grown in a temperate climate. *Energy*, *320*, 135433. https://doi.org/https://doi.org/10.1016/j.energy.2025.135433
6. Du, S., Yang, H., Qian, K., Wang, X., Chen, H. (2014). Fusion and transformation properties of the inorganic components in biomass ash. *Fuel*, *117*, 1281–1287. https://doi.org/https://doi.org/10.1016/j.fuel.2013.07.085
7. Gaurav, G. K., Mehmood, T., Cheng, L., Klemeš, J. J., Shrivastava, D. K. (2020). Water hyacinth as a biomass: A review. *Journal of Cleaner Production*, *277*, 122214. https://doi.org/https://doi.org/10.1016/j.jclepro.2020.122214
8. He, H., Wang, Y., Sun, W., Sun, Y., Wu, K. (2024).

Effects of different biomass feedstocks on the pelleting process and pellet qualities. *Sustainable Energy Technologies and Assessments*, *69*, 103912. https://doi.org/https://doi.org/10.1016/j.seta.2024.103912

9. He, Z., Liu, S., Wang, S., Liu, W., Li, Y., Feng, X. (2022). Reduced pollutant emissions and slagging rate of biomass pellet combustion by optimizing the multilayer distribution of secondary air. *ACS Omega*, *7*(33), 28962–28973. https://doi.org/https://doi.org/10.1021/acsomega.2c02587
10. Hedayati, A., Falk, J., Borén, E., Lindgren, R., Skoglund, N., Boman, C., Öhman, M. (2022). Ash Transformation during fixed-bed combustion of agricultural biomass with a focus on potassium and phosphorus. *Energy & fuels*, *36*(7), 3640–3653. https://doi.org/https://doi.org/10.1021/acs.energyfuels.1c04355
11. Hrbek, J., Oberndorfer, C., Zanzinger, P., Pfeifer, C. (2021). Influence of $Ca(OH)_2$ on ash melting behaviour of woody biomass. *Carbon Resources Conversion*, *4*, 84–88. https://doi.org/https://doi.org/10.1016/j.crcon.2021.01.008
12. Hu, Y., Meng, J., Liu, Z., Yue, H., Zhang, X., Zhang, Y., Chen, R. (2023). Comprehensive combustion performances of water hyacinth and pistia stratiotes pellet fuels. *CLEAN – Soil, Air, Water*, *51*(4), 2100230. https://doi.org/https://doi.org/10.1002/clen.202100230
13. Johansen, J. M., Jakobsen, J. G., Frandsen, F. J., Glarborg, P. (2011). Release of K, Cl, and S during pyrolysis and combustion of high-chlorine biomass. *Energy & fuels*, *25*(11), 4961–4971. https://doi.org/https://doi.org/10.1021/ef201098n
14. Kaknics, J., Michel, R., Poirier, J. (2016). Miscanthus ash transformation and interaction with bed materials at high temperature. *Fuel Processing Technology*, *141*, 178–184. https://doi.org/https://doi.org/10.1016/j.fuproc.2015.08.041
15. Król, D., Motyl, P., & Poskrobko, S. (2022). Chlorine corrosion in a low-power boiler fired with agricultural biomass. *Energies*, *15*(1), 382. https://doi.org/https://doi.org/10.3390/en15010382
16. Kuswa, F. M., Putra, H. P., Prabowo, Darmawan, A., Aziz, M., Hariana, H. (2024). Investigation of the combustion and ash deposition characteristics of oil palm waste biomasses. *Biomass Conversion and Biorefinery*, *14*(19), 24375–24395. https://doi.org/https://doi.org/10.1007/s13399-023-04418-z
17. Lachman, J., Baláš, M., Lisý, M., Lisá, H., Milčák, P., Elbl, P. (2021). An overview of slagging and fouling indicators and their applicability to biomass fuels. *Fuel Processing Technology*, *217*, 106804. https://doi.org/https://doi.org/10.1016/j.fuproc.2021.106804
18. Lara-Serrano, J. S., Rutiaga-Quiñones, O. M., López-Miranda, J., Fileto-Pérez, H. A., Pedraza-Bucio, F. E., Rico-Cerda, J. L., Rutiaga-Quiñones, J. G. (2016). Physicochemical characterization of water hyacinth (*Eichhornia crassipes* (Mart.) Solms). *BioResources*, *11*(3), 7214–7223. https://doi.org/https://doi.org/10.15376/biores.11.3.7214-7223
19. Li, F., He, X., Srishti, A., Song, S., Tan, H. T. W., Sweeney, D. J., Ghosh, S., Wang, C.-H. (2021). Water hyacinth for energy and environmental applications: A review. *Bioresource Technology*, *327*, 124809. https://doi.org/https://doi.org/10.1016/j.biortech.2021.124809
20. Li, F., Yu, B., Zhao, W., Wang, J., Xu, M., Fan, H., Huang, J., Fang, Y. (2022). Investigation on formation mechanisms of ash and deposit from cotton stalk vibrating grate boiler combustion based on their characteristics. *Fuel*, *323*, 124446. https://doi.org/https://doi.org/10.1016/j.fuel.2022.124446
21. Luan, J., Wang, Q., Shao, D., Cui, B., Han, P., He, Q. (2025). Research progress on influencing factors and control methods of slagging in biomass combustion [Review]. *Frontiers in Energy Research*, *13*. https://doi.org/https://doi.org/10.3389/fenrg.2025.1634354
22. Mack, R., Schön, C., Kuptz, D., Hartmann, H., Brunner, T., Obernberger, I., Behr, H. M. (2024). Influence of wood species and additives on emission behavior of wood pellets in a residential pellet stove and a boiler. *Biomass Conversion and Biorefinery*, *14*(17), 20241–20260. https://doi.org/https://doi.org/10.1007/s13399-023-04204-x
23. Marczak, H. (2020). Analysis of energy consumption in the production chain of heat from pellet. *Advances in Science and Technology Research Journal*, *14*(2), 206–214. https://doi.org/https://doi.org/10.12913/22998624/118868
24. Mörtenkötter, H., Kulkarni, M., Fuchs, L., Kerscher, F., Fendt, S., Spliethoff, H. (2024). Effects of aluminosilicate-based additives on potassium release and ash melting during biomass combustion. *Fuel*, *374*, 132471. https://doi.org/https://doi.org/10.1016/j.fuel.2024.132471
25. Onyari, E. K., Fayomi, G. U., Jaiyeola, A. T. (2024). Unveiling the situation of water hyacinth on fresh water bodies in Nigeria and South Africa: Management, workable practices and potentials. *Case Studies in Chemical and Environmental Engineering*, *10*, 100974. https://doi.org/https://doi.org/10.1016/j.cscee.2024.100974
26. Pio, D. T., Tarelho, L. A. C., Nunes, T. F. V., Baptista, M. F., Matos, M. A. A. (2020). Co-combustion of residual forest biomass and sludge in a pilot-scale bubbling fluidized bed. *Journal of Cleaner Production*, *249*, 119309. https://doi.org/https://doi.org/10.1016/j.jclepro.2019.119309
27. Rabaçal, M., Fernandes, U., Costa, M. (2013). Combustion and emission characteristics of a domestic

boiler fired with pellets of pine, industrial wood wastes and peach stones. *Renewable Energy*, *51*, 220–226. https://doi.org/https://doi.org/10.1016/j.renene.2012.09.020

28. Racero-Galaraga, D., Rhenals-Julio, J. D., Sofan-German, S., Mendoza, J. M., Bula-Silvera, A. (2024). Proximate analysis in biomass: Standards, applications and key characteristics. *Results in Chemistry*, *12*, 101886. https://doi.org/https://doi.org/10.1016/j.rechem.2024.101886
29. Ríos-Badrán, I. M., Luzardo-Ocampo, I., García-Trejo, J. F., Santos-Cruz, J., Gutiérrez-Antonio, C. (2020). Production and characterization of fuel pellets from rice husk and wheat straw. *Renewable Energy*, *145*, 500–507. https://doi.org/https://doi.org/10.1016/j.renene.2019.06.048
30. Smołka-Danielowska, D., Jabłońska, M. (2022). Chemical and mineral composition of ashes from wood biomass combustion in domestic wood-fired furnaces. *International Journal of Environmental Science and Technology*, *19*(6), 5359–5372. https://doi.org/https://doi.org/10.1007/s13762-021-03506-9
31. Sommersacher, P., Brunner, T., Obernberger, I. (2012). Fuel indexes: A novel method for the evaluation of relevant combustion properties of new biomass fuels. *Energy & fuels*, *26*(1), 380–390. https://doi.org/https://doi.org/10.1021/ef201282y
32. Stanisławski, R., Robert, J., Nitsche, M. (2022). Reduction of the CO emission from wood pellet small-scale boiler using model-based control. *Energy*, *243*, 123009. https://doi.org/https://doi.org/10.1016/j.energy.2021.123009
33. Sukarta, I. N., Sastrawidana, I. D. K., Budiarsa Suyasa, I. W. (2023). Proximate analysis and calorific value of fuel briquettes from wood and coffee skins biomass as a renewable energy source. *Ecological Engineering & Environmental Technology*, *24*(8), 293–300. https://doi.org/https://doi.org/10.12912/27197050/172506
34. Trinh, V. T., Lee, B.-H., Jeon, C.-H. (2024). Prediction of ash deposition in a biomass boiler using thermomechanical analysis. *Journal of Industrial and Engineering Chemistry*, *131*, 481–489. https://doi.org/https://doi.org/10.1016/j.jiec.2023.10.052
35. Vassilev, S. V., Vassileva, C. G., Song, Y.-C., Li, W.-Y., Feng, J. (2017). Ash contents and ash-forming elements of biomass and their significance for solid biofuel combustion. *Fuel*, *208*, 377–409. https://doi.org/https://doi.org/10.1016/j.fuel.2017.07.036
36. Wang, H., Zhou, T., Tan, X., Hu, N., Wang, Y., Yang, H., Zhang, M. (2024). Experimental study on the sintering characteristics of biomass ash. *Fuel*, *356*, 129586. https://doi.org/https://doi.org/10.1016/j.fuel.2023.129586
37. Weber, R., Poyraz, Y., Mancini, M., Schwabauer, A. (2021). Biomass fly-ash deposition: Dependence of deposition rate on probe/particle temperature in 115–1200 °C range. *Fuel*, *290*, 120033. https://doi.org/https://doi.org/10.1016/j.fuel.2020.120033
38. Wu, H., Castro, M., Jensen, P. A., Frandsen, F. J., Glarborg, P., Dam-Johansen, K., Røkke, M., & Lundtorp, K. (2011). Release and Transformation of Inorganic Elements in Combustion of a High-Phosphorus Fuel. *Energy & fuels*, *25*(7), 2874–2886. https://doi.org/https://doi.org/10.1021/ef200454y
39. Yilmaz, D., Steenari, B.-M., Leion, H. (2021). Comparative study: Impacts of Ca and Mg salts on iron oxygen carriers in chemical looping combustion of biomass. *ACS Omega*, *6*(25), 16649–16660. https://doi.org/https://doi.org/10.1021/acsomega.1c02138
40. Yue, H., Rao, Y., Meng, J., Zhang, X., Chen, R. (2025). Gas emissions from combustion of water hyacinth and pistia stratiotes biomass particles under O_2/CO_2. *Energy Sources, Part A: Recovery, Utilization, and Environmental Effects*, *47*(1), 2760–2774. https://doi.org/https://doi.org/10.1080/15567036.2020.1843568
41. Zhang, F., Hou, X., Xue, X., Ren, J., Dong, L., Wei, X., Jian, L., Deng, L. (2023). Release characteristics of potassium during biomass combustion. *Energies*, *16*(10), 4107. https://www.mdpi.com/1996-1073/16/10/4107
42. Zhang, H., Yu, C., Luo, Z. (2020). Investigation of ash deposition dynamic process in an industrial biomass CFB boiler burning high alkali and chlorine fuel. *RSC Advances*, *10*(36), 21420–21426. https://doi.org/https://doi.org/10.1039/D0RA04370B